Defect-Induced Photoluminescence in Monolayer Semiconducting Transition Metal Dichalcogenides

Philippe K. Chow,[†] Robin B. Jacobs-Gedrim,[‡] Jian Gao,[†] Toh-Ming Lu,[§] Bin Yu,[‡] Humberto Terrones,[§] and Nikhil Koratkar*[,†,∥]

[†]Materials Science and Engineering, Rensselaer Polytechnic Institute, Troy, New York 12180, United States, [‡]SUNY College of Nanoscale Science and Engineering, Albany, New York 12203, United States, [§]Physics, Applied Physics, and Astronomy, Rensselaer Polytechnic Institute, Troy, New York 12180, United States, and [∥]Mechanical, Aerospace and Nuclear Engineering, Rensselaer Polytechnic Institute, Troy, New York 12180, United States

ABSTRACT It is well established that defects strongly influence properties in two-dimensional materials. For graphene, atomic defects activate the Raman-active centrosymmetric A_{1g} ring-breathing mode known as the D-peak. The relative intensity of this D-peak compared to the G-band peak is the most widely accepted measure of the quality of graphene films. However, no such metric exists for monolayer semiconducting transition metal dichalcogenides such as WS_2 or MoS_2. Here we intentionally create atomic-scale defects in the hexagonal lattice of pristine WS_2 and MoS_2 monolayers using plasma treatments and study the evolution of their Raman and photoluminescence spectra. High-resolution transmission electron microscopy confirms plasma-induced creation of atomic-scale point defects in the monolayer sheets. We find that while the Raman spectra of semiconducting transition metal dichalcogenides (at 532 nm excitation) are insensitive to defects, their photoluminescence reveals a distinct defect-related spectral feature located ~0.1 eV below the neutral free A-exciton peak. This peak originates from defect-bound neutral excitons and intensifies as the two-dimensional (2D) sheet is made more defective. This spectral feature is observable in air under ambient conditions (room temperature and atmospheric pressure), which allows for a relatively simple way to determine the defectiveness of 2D semiconducting nanosheets. Controlled defect creation could also enable tailoring of the optical properties of these materials in optoelectronic device applications.

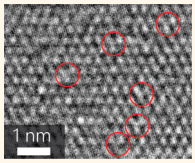

KEYWORDS: transition metal dichalcogenides · monolayer · defects · photoluminescence · excitons

Two-dimensional (2D) single-layer semiconducting group VI transition metal dichalcogenides (TMDs) exhibit remarkably enhanced interaction with visible light due to an indirect-to-direct band-gap conversion at the monolayer limit,[1−3] making these materials attractive for nanoscale optical device applications.[4,5] Reduced dielectric charge screening, due to quantum confinement effects in 2D structures, results in stronger excitonic interactions, rendering these systems versatile platforms for studying light−matter interactions.[6−9] The enhanced sensitivity of the optoelectronic properties of monolayer TMD materials to the surrounding dielectric environment also provides an additional handle to optimize these materials for ultrathin transistor[10] and chemical sensor[11] applications.

Given the variety of possible applications of TMDs, it is important to develop a simple and nondestructive method for characterizing the defect state of semiconducting TMD materials. Such a method has been established for graphene, a 2D network of sp^2-bonded carbon, in which atomic defects activate the Raman-active centrosymmetric A_{1g} ring-breathing mode known in the literature as the D-peak.[12] The intensity ratio of the Raman D to G band peak in graphene (*i.e.*, I_D/I_G ratio)[12,13] is now widely utilized as a metric to quantify the quality of monolayer and few-layered graphene films. However, a similar method to characterize the quality of 2D semiconducting TMDs is completely lacking. One group has reported the appearance of a defect-activated photoluminescence (PL) spectral feature in mechanically exfoliated TMD monolayers at low temperatures (77 K) and under a partial pressure of nitrogen gas.[14] However, in their measurements, such defect-related photoluminescence features were absent at room temperature, and it is unclear how the intensity of this feature correlated to defectiveness of the sheet (Supplementary Figure S1).

* Address correspondence to koratn@rpi.edu.

Received for review October 22, 2014 and accepted January 20, 2015.

Published online January 20, 2015
10.1021/nn5073495

Presently, sample quality in as-grown TMD nanolayers is established using high-resolution transmission electron microscopy or by electrical transport measurements, which are complex and time-consuming and/or involve establishing electrical contacts to the sample. Consequently, there is a need to develop simple and reliable approaches to assess the quality of TMD samples *via* noncontact and nondestructive measurements that can be rapidly performed under ambient conditions. To address this issue, we studied the role of defects on the PL and Raman spectra of mechanically exfoliated tungsten disulfide (WS_2) and molybdenum disulfide (MoS_2) monolayers as a prototypical material system. Defects were introduced in the monolayer sheets by argon plasma treatment. As a general trend, we observed both neutral and charged excitons (*i.e.*, trions) in the untreated samples. With successive plasma treatments, we observed a new defect-related spectral feature located ~0.1 eV below the A-exciton emission peak that consistently grows in intensity with plasma treatment. The PL and Raman measurements carried out in this study were performed in air under ambient conditions (room temperature and atmospheric pressure). High-resolution transmission electron microscopy measurements confirmed the generation of atomic-scale defects in the hexagonal TMD lattice when subjected to plasma treatment. Such defect-induced photoluminescence in air at room temperature and atmospheric pressure is unusual and highlights the richness and magnitude of exciton−defect interactions in semiconducting monolayer TMDs.

RESULTS AND DISCUSSION

WS_2 and MoS_2 monolayers were mechanically exfoliated from commercially available bulk single crystals (2D Semiconductors, WS_2; Ward's Science, MoS_2) onto ~285 nm thick SiO_2 on n^{++}-type silicon wafers (Silicon Quest International, Inc.) that were previously washed in acetone and 2-propanol and dried with ultra-high-purity nitrogen. The wafers were additionally cleaned by UV/ozone treatment for ~10 min before exfoliation. Monolayer regions were identified with confocal optical microscopy by their white-light optical reflectance contrast against the bare substrate as well as Raman/PL measurements using a WITec alpha300R spectrometer equipped with a 532 nm excitation line and Si-based CCD detector (1800 g/mm) in a backscattering geometry. By using an ~1−2 μm laser spot, we carefully ensured that our optical measurements were collected from homogeneous regions of the monolayer to avoid effects from edges and few-layer regions. To minimize sample heating effects, we used laser powers less than 40 μW for all the experiments.

We first describe our results for the exfoliated WS_2 monolayers (shown in Figure 1c), which exhibit strong

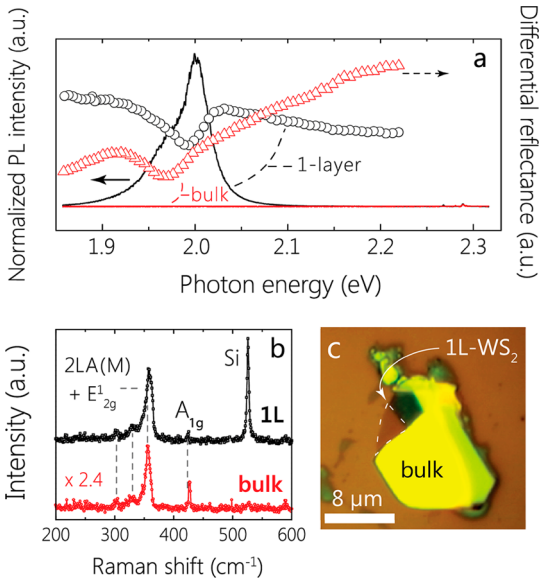

Figure 1. (a) Photoluminescence ($\lambda_{exc} \approx 532$ nm, $P_{laser} = 5 \pm 1$ μW, solid lines, left axis) and differential reflectance (symbols, right axis) spectra from mechanically exfoliated bulk (red lines and triangles) and single-layer (black lines, circles) WS_2 flakes shown in (c). Spectra are normalized to the integrated intensities of the 2LA(M) and E^1_{2g} bands to highlight PL intensity differences. (b) Similarly normalized Raman spectra from single-layer (top) and bulk (bottom) WS_2 showing a clear WS_2 Raman peak ratio difference. (c) Optical micrograph of the WS_2 flake.

(orders of magnitude more intense than Raman peaks) room-temperature PL relative to bulk WS_2 and a small Stokes shift (Figure 1a). The WS_2 Raman 2LA(M) and E^1_{2g} bands from the bulk and monolayer samples exhibit expected peak positions and intensity ratios (Figure 1b) as previously reported by others.[15,16] The observed ~30 meV blue-shift in the differential reflectance peak upon moving from bulk to single-layer WS_2 (1L-WS_2) is consistent with previous experimental and theoretical reports and stems from exciton confinement effects, which cause a slight increase in the K-point energy gap.[3,17] The PL spectra from 1L-WS_2 is dominated by free neutral A-exciton emission (simply denoted, X^O for WS_2) near ~2.01 eV.[18,19] The B-exciton, arising from the spin−orbit split valence band, is not observed due to the PL detector range. A significant low-energy tail to the main PL feature was observed in all of our exfoliated monolayer WS_2 samples, which we attribute to charged exciton (trion, X^T) emission. This could result from residual charge doping[20,21] or from charged impurites,[22] due to strain[23] or impurity doping from chemical vapor transport agents (such as I_2 or Br_2) that are commonly used to grow commercially available bulk single-crystal WS_2.[17]

To study the role of defects on the PL spectrum of monolayer WS_2, we systematically investigated the PL spectral evolution (Figure 2) after successive ion bombardment treatments and exposure to air. We subjected the samples to successive 5 s treatments in a ~25 W argon plasma (Fischione Instruments,

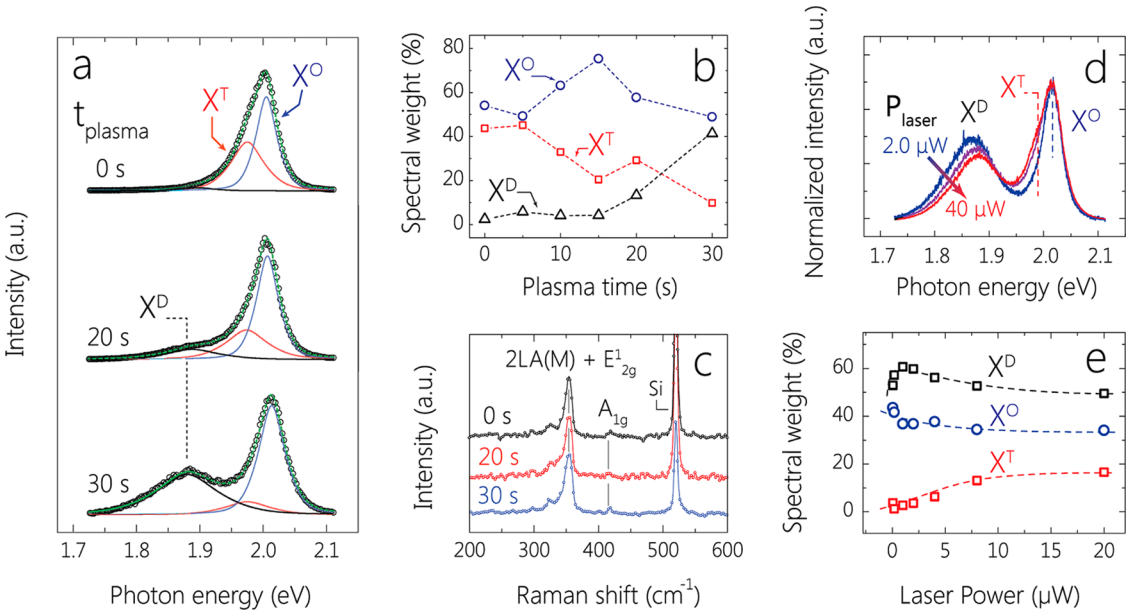

Figure 2. (a) Representative PL spectra (normalized to the total integrated PL intensity) from exfoliated WS_2 monolayers as a function of plasma treatment time. Curve fitting reveals neutral (X^O), charged (X^T), and defect-related (X^D) spectral contributions. (b) Curve fitting results for the three spectral contributions as a function of plasma time. (c) Representative Raman spectra with increasing plasma treatment time. (d) Excitation power-dependent PL measurements from the defective monolayer sample. (e) Spectral weight of the neutral (X^O), charged (X^T), and defect-related (X^D) spectral PL contributions as a function of laser power.

Nanoclean model 1070) at ~200 mTorr. Micro-PL and Raman spectra were measured within a few minutes of each plasma treatment on the same monolayer region. We studied the evolution of exciton interactions by curve fitting of the PL spectra. The optimal line shape for all spectral contributions was a mixed Gaussian–Lorentzian function with 83% Lorentzian character. Figure 2a shows representative WS_2 PL spectra from a series of plasma treatment times, with each normalized to the total integrated PL intensity. Such normalization was used to highlight the PL line shape change. While initially dominated by X^O and X^T emission, a new spectral feature arises near ~1.90 eV with increased plasma treatment.

We attribute this feature to excitons bound to defects (X^D) that were created by the ion bombardment. Similar subgap defect-related peaks have been observed in certain quantum-confined systems such as quantum-well structures[24] and nanostructured ZnO[25] materials but never reported for TMD monolayers at room temperature.

Figure 2b shows the change in individual PL spectral contributions, obtained from curve fitting, for the WS_2 sample with successive plasma treatments. We observed two regimes within the extent of our plasma treatment study. During the first half of the treatment, the PL is dominated by X^O and X^T emission. The increase (decrease) in X^O (X^T) emission along with low X^D intensity suggests irradiation-induced conversion from charged to neutral exciton emission. As the untreated monolayer is likely electron-doped, typical of exfoliated MoS_2[11,20] and WS_2[31] on SiO_2 substrates, the interaction between defects and the ambient chemistry (*i.e.*, O_2, N_2, H_2O) could serve to dope the crystal toward the opposite polarity (*e.g.*, hole doping).[14,26] Such a compensation doping process would reduce the free carrier concentration and, therefore, the spectral weight of the charged exciton peak, X^T. The slight increase in the PL intensity during the first 15 s of treatment (Supplementary Figure S2) is also in agreement with this compensation doping mechanism. After approximately 15 s of plasma treatment, the X^D peak rises rapidly, while the X^O and X^T peaks decrease markedly in weight. We provide data from another WS_2 sample in Supplementary Figures S3 and S4 to further confirm this trend for X^D growth with plasma irradiation time. Note that we did not observe changes in the Raman spectra, collected using 532 nm excitation, as a function of plasma treatment time (Figure 2c). Additional testing over a wide range of wavelengths is necessary to conclusively establish whether or not defects affect the Raman spectra of monolayer TMD materials. Unlike a previous report,[14] we observe the defect-induced X^D peak in air at room temperature and atmospheric pressure, which clearly increases in spectral weight with irradiation time.

We explored the origin of the PL spectral features by examining the excitation power (P_{laser}) dependence of the PL spectrum (Figure 2d,e) from the defective WS_2 monolayer. Peak-normalized spectra and curve-fitting results are shown in Figure 2d and e, respectively. The X^D peak contribution initially rises to a maximum (Figure 2e) and then decreases, suggesting defect site saturation with trapped excitons. The presence of the

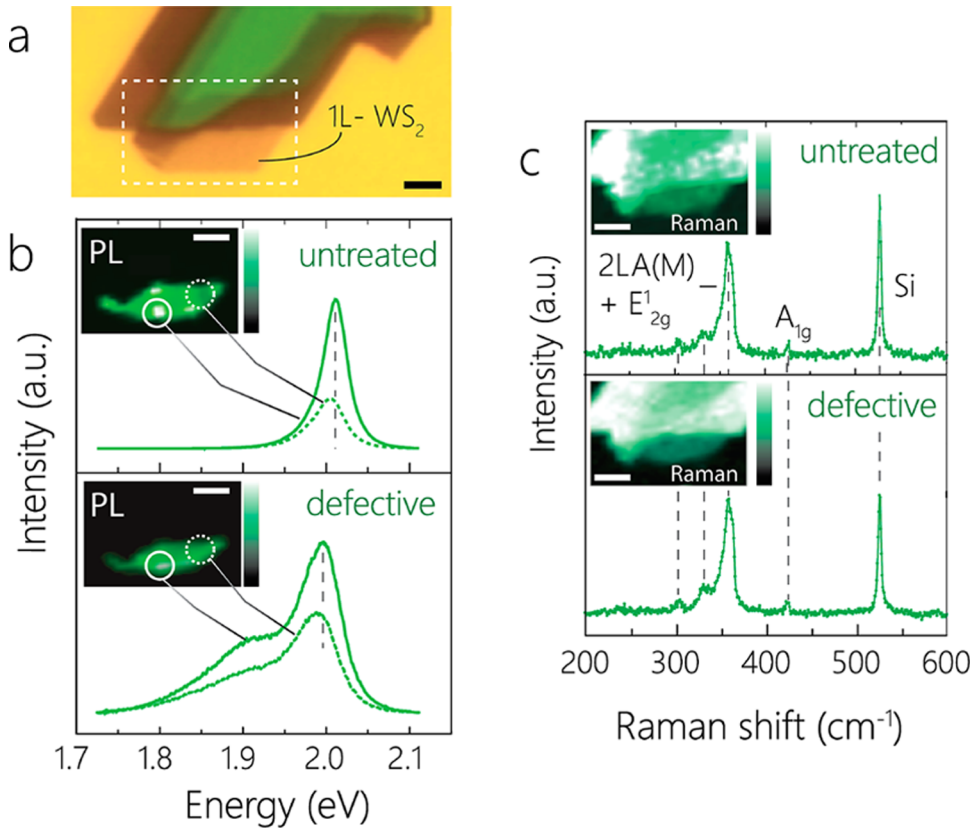

Figure 3. (a) Optical micrograph of the WS_2 flake used for PL and Raman mapping. The scale bar indicates 4 μm. (b) Integrated PL intensity map (inset) from the dashed rectangular region in (a) for the untreated (top) and plasma-treated (bottom) WS_2 flakes. The individual pixels are smoothed using linear interpolation. The color scale indicates intensity with arbitrary units. Spectra with solid lines are from the region circled in the PL map with a solid circle. Dashed-line spectra are from the region encircled by a dashed line. Plasma treatment was performed for ~30 s. Scale bar indicates 2 μm. (c) Raman peak intensity map (inset) from the combined 2LA(M) and E^1_{2g} mode from untreated (top) and plasma-treated (bottom) WS_2 flake. Raman spectra shown here are from the monolayer region only. The scale bar indicates 2 μm.

X^D feature without significant X^T contribution suggests that excitons bound to defects are charge-neutral. We also observed a ~10 meV blue-shift in the X^D peak emission energy at low laser powers, which tends toward an eventual plateau with excitation power. This blue-shift is inconsistent with increased photocarrier screening of excitons, which should cause an increase in the energy of all PL peaks due to a decreased exciton binding energy in the monolayer. This effect may stem from mutual interaction between the defect-bound excitons, but further work is necessary to understand this phenomenon. We additionally point out that the X^D peak does not result from radiative transitions associated with impurity levels in the 2D semiconductor. This is because our defect-free samples displayed a large trion (X^T) spectral contribution (likely due to impurities) but did not exhibit the X^D feature. This suggests that the plasma treatment induces radiative defect states with distinctly lower energy than the optical band-gap value for untreated layers. The spectral location of the X^D peak below the free and charged exciton emission indicates that defects created by our plasma treatment act as exciton traps, effectively reducing the electron−hole pair interaction. It should also be noted that the X^T spectral contribution clearly increases with excitation power, as indicated in Figure 2d,e. This is the expected behavior of trions, as formation of a charged three-body state is more probable at high photoexcited carrier densities. The greater line width of the X^D peak (fwhm ~0.12 eV) than the X^T (~0.08 eV) or X^O (~0.05 eV) indicates a more continuous energy distribution, probably due to the fact that defects created by plasma bombardment are likely inhomogeneous and therefore do not give rise to a sharply defined energy level.

We studied the spatial extent of the plasma-induced defect signatures by measuring the PL and Raman spectra as a function of the position of the excitation laser spot on a separate WS_2 flake, shown in the optical micrograph in Figure 3a. The integrated PL intensity map (Figure 3b, inset) for the untreated WS_2 flake shows contrast that stems only from the light brown monolayer region in Figure 3a (this is to be expected since only the monolayer displays a large PL response). The top portion of Figure 3b shows example spectra from regions of strong (solid line corresponds to spectrum from solid circle region in PL map) and weaker (dashed circle) PL intensity. The nonuniformity

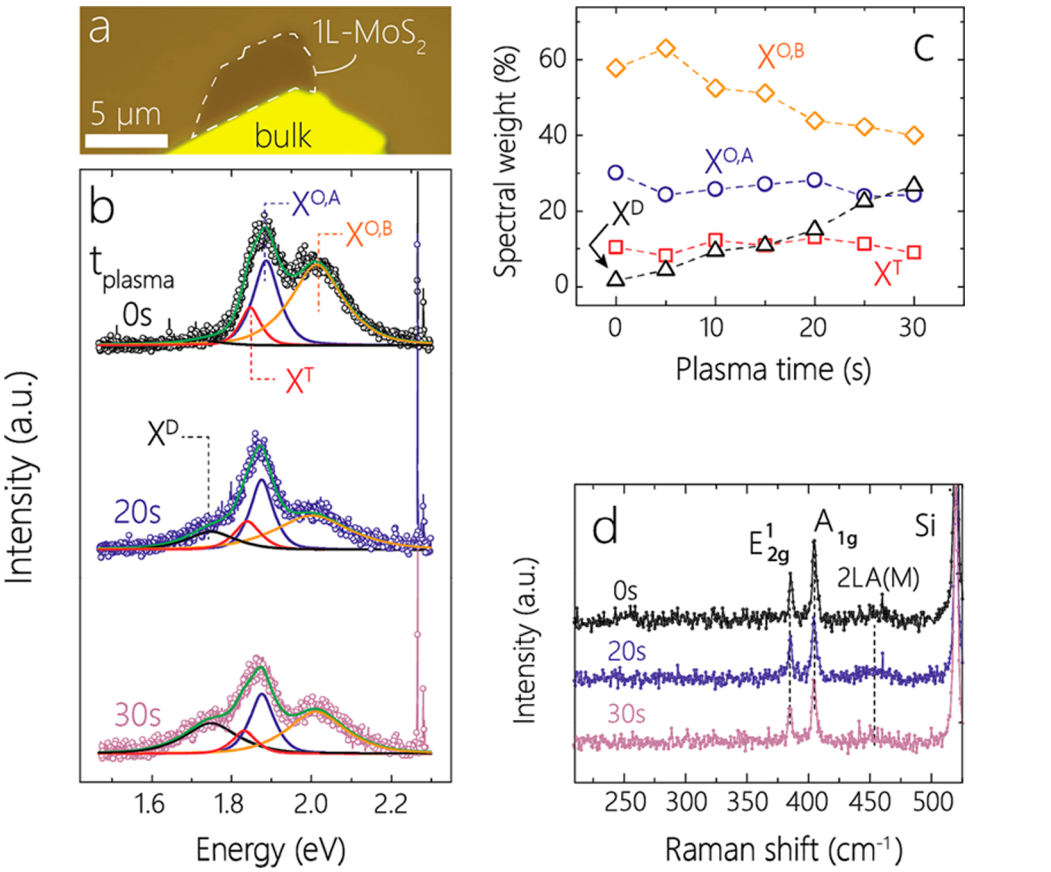

Figure 4. (a) Optical micrograph of the mechanically exfoliated MoS_2 flake used for PL and Raman study. (b) Representative photoluminescence spectra (P_{laser} = 5 ± 1 μW) for the exfoliated MoS_2 monolayer (normalized to the total integrated PL intensity) for various plasma treatment times with curve-fitting results. Curve fitting reveals contributions from the B-exciton ($X^{O,B}$), A-exciton ($X^{O,A}$), charged exciton (X^T), and defect-related (X^D) spectral contributions. (c) Spectral weight of the four PL peak contributions as a function of plasma treatment time for the complete data set. (d) Representative Raman spectra showing the dominant MoS_2 Raman modes and no change in peak position with plasma treatment.

in the PL intensity is likely due to natural doping variations in the monolayer, as we observe larger trion (X^T) contribution (low-energy PL shoulder) in regions with weaker PL intensity. We repeated the analyses of the PL spatial variation for the same sample after plasma exposure. The absolute intensity of the integrated PL intensity is diminished by plasma treatment, but still strongly emanates exclusively from the monolayer region (inset Figure 3b, bottom). This indicates that the plasma treatment does not induce any photoluminescence in multilayer regions of the flake. PL spectra from the defective WS_2 clearly show (Figure 3b, bottom) a significant defect-induced contribution (X^D) near 1.9 eV, despite variations in PL intensity, for all pixels in the defective WS_2 monolayer map. This indicates that the plasma bombardment created defect signatures over the entire monolayer flake within our spatial resolution (~1−2 μm). Variations in PL intensity, as observed for the untreated WS_2, was also observed in the defective sample, indicating that the natural doping profile in the untreated monolayer is preserved to an observable extent despite defect creation.

We also studied the spatial variation of the 532 nm excitation Raman spectra by mapping the peak intensity of the convoluted 2LA(M) and E^1_{2g} modes (Figure 3c, insets). As expected, the Raman maps for the untreated and defective sample show weaker intensity in the monolayer compared to the few-layer regions, as is commonly observed for MoS_2 and WS_2.[1,16] Representative Raman spectra, taken from the monolayer regions, are shown in the main portions of Figure 3c, which indicate that the plasma treatment does not affect the Raman spectra within our spectral resolution. These data, and our results shown in Figure 2, further confirm the dominant effect of the defect treatment on PL rather than on the Raman spectra under 532 nm excitation used here.

We also created defects in exfoliated monolayer MoS_2 flakes on SiO_2/Si substrates using the same argon plasma treatments as those employed for WS_2. Figure 4 shows representative PL spectra, normalized to the total integrated PL intensity, for the MoS_2 flake shown in Figure 4a for different plasma treatment times. The lower PL intensity than for the case of WS_2 films is due to the lower PL efficiency of MoS_2 monolayers.[1,27] We limited

our excitation power to 5 μW, above which we observed laser-induced spectral changes in defective samples.

We similarly employed curve fitting using mixed Gaussian–Lorentzian curves to deconvolute the PL spectra. The large and broad contribution near 2.01 eV stems from B-exciton emission ($X^{O,B}$) from the spin–orbit split valence band at the K-points of the Brillouin zone.[1] This peak is absent in the WS_2 spectrum due to its larger spin–orbit splitting than MoS_2.[7] In addition to this contribution, we model the PL spectra using the same contributions as in the case of WS_2 including the neutral free A-exciton near 1.89 eV ($X^{O,A}$), the negatively charged trion (X^T),[20] and finally, a defect-induced feature (X^D). Figure 4b,c shows the evolution of the spectral distribution from the curve-fitting results for each successive plasma treatment. As in the case of WS_2, we clearly observed the emergence of a low-energy feature with successive plasma treatments, which we assign to defect-induced PL. Interestingly, however, we note a monotonic decrease in the $X^{O,B}$ spectral weight with monotonically increasing X^D weight (Figure 4c). Additionally, the $X^{O,A}$ and X^T weights change less dramatically than in the case of WS_2. This could result from an increased preference toward recombination of photogenerated excitons *via* a lower-energy defect-assisted mechanism.

Similar to the case of WS_2, the Raman spectra collected using 532 nm excitation (shown in Figure 4d) remain unchanged within our experimental resolution. The E^1_{2g} and A_{1g} peaks show no detectable shift in position or relative intensity. We acknowledge another study[32] in which, using oxygen plasma, the authors demonstrated strong PL quenching in exfoliated MoS_2 monolayers as well as an oxidation-induced Raman feature near 225 cm^{-1} under 532 nm excitation. However, no defect-related PL feature was reported. We believe that this particular study involved more aggressive plasma irradiation than used in our work here, where the PL spectral changes, as observed in this work, are largely masked by drastic decreases in PL efficiency due to nonradiative exciton recombination. Additionally, the laser power densities used were 2 orders of magnitude higher than those in this work, bringing about the possibility of differences in laser–sample interactions. The defect-dependent PL and Raman results from exfoliated MoS_2 monolayers confirm the conclusions drawn from WS_2.

To obtain an atomistic understanding of the effects of our plasma treatment on the crystallinity of TMD monolayers, we performed high-resolution transmission electron microscopy (HR-TEM) analysis of pristine and defective WS_2 monolayers. We employed a polymer-free transfer method (Materials and Methods section) to prepare suspended monolayer WS_2 samples for HR-TEM imaging (Figure 5a). Whereas the untreated samples (Figure 5b) exhibit a highly crystalline structure ($d_{\{1000\}} \approx 0.34$ nm), those treated by ion

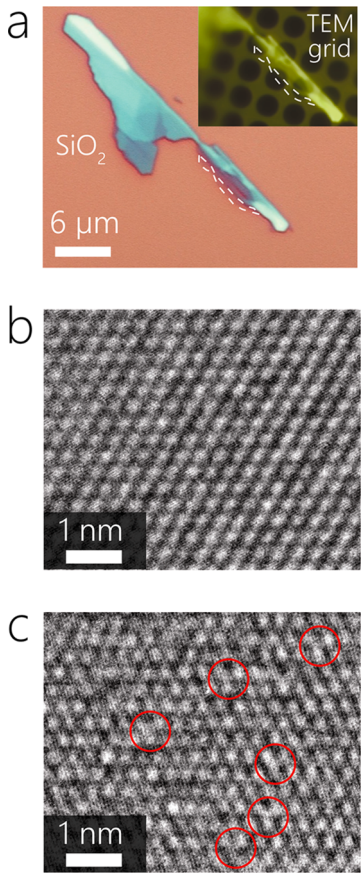

Figure 5. (a) Optical micrograph of the WS_2 flake used for high-resolution-TEM (HR-TEM) imaging with the monolayer region indicated by a dotted line. The inset shows the same flake after a polymer-free transfer to the TEM grid (see Materials and Methods). (b) HR-TEM image of the as-transferred (untreated) monolayer WS_2 film. (c) HR-TEM image of the same monolayer WS_2 sample after ~10 s of plasma irradiation treatment. The generation of atomic-scale point defects in the WS_2 lattice is highlighted by the red circles.

bombardment clearly show signs of damage, containing many defect sites (indicated by red circles in Figure 5c). The highlighted defects appear as points of moderate contrast between three bright spots. These features are characteristic of the phase contrast from single-vacancy defects and are the result of a single sulfur or tungsten atom missing from the otherwise complete hexagonal WS_2 lattice.[3] To determine whether we are generating sulfur or tungsten vacancies, we performed TEM simulations by using the same settings that were employed in the HRTEM measurements. More specifically, we simulated sulfur single-vacancy, tungsten single-vacancy, and sulfur divacancy configurations. The results (Supplementary Figure S5) indicate that the pattern of points of moderate contrast between three bright spots is best represented by a sulfur single vacancy. It should be noted that such sulfur vacancies could also interact with foreign gas species during air exposure. Despite these obvious differences with ion bombardment, we

see that the hexagonal WS_2 lattice is mostly preserved. This could help explain why the Raman signatures are largely unchanged throughout our plasma treatment study. We mention that we did not observe electron irradiation effects with our non-plasma-treated TEM samples while using a 200 keV beam energy even after long exposure times (>20 min), similar to other reports.[28,29] Interestingly, others[30] have reported noticeable irradiation effects at 80 keV in MoS_2, suggesting a nonmonotonic energetic cross-section for electron knock-on damage. We did, however, observe some irradiation effects in the TEM sample after plasma treatment, such as defect migration.[30] In general, we found that the imaging quality was the highest and beam-induced structural changes were minimal when imaging far from large-scale structural defects such as monolayer sheet edges or tears in the TMD sheet.

CONCLUSIONS

In summary, we have explored the effect of atomic-scale point defects, created by simple plasma treatments, on the PL spectra of semiconducting TMD monolayers. We report the evolution of a distinct defect-related spectral feature located ~0.1 eV below the A-exciton peak in the disulfides of tungsten and molybdenum (WS_2, MoS_2) prepared by mechanical exfoliation. As exemplified by our study, interactions between atomic-scale defects and excitons in monolayer (semiconducting) TMDs occur with sufficient strength in air at room temperature and atmospheric pressure to enable the evolution of the aforementioned defect-related peak in the PL spectra. We found that the Raman spectra of the TMD monolayers are not as sensitive to the defects compared to a photoluminescence spectrum under 532 nm excitation. Our high-resolution electron microscopy study provides atomistically resolved evidence of plasma-induced point defects in the monolayer lattice, suggesting their role in the defect-related PL feature. This feature could be used as a sensitive indicator of the "state of defectiveness" of semiconducting TMD nanosheets. The evolution of a new extrinsically induced defect state in the band gap brings to light largely unexplored opportunities for tailoring the optoelectronic properties of two-dimensional semiconducting TMDs through control of defect density, type, and distribution.

MATERIALS AND METHODS

Raman and Photoluminescence Spectroscopy. Raman and PL spectroscopy were performed using a WITec alpha300R spectrometer equipped with a 532 nm excitation line and CCD detector in a backscattering geometry. To minimize sample heating effects, laser powers of less than 40 μW were used for all the experiments. All measurements were performed in air at ~25 °C and atmospheric pressure.

Differential Reflectance and Optical Microscopy Measurements. Differential reflectance measurements were performed using an LED white light source by measuring the difference in reflected intensity from the WS_2/SiO_2 and bare silicon wafer substrate and normalizing this to the substrate-reflected intensity. For optical microscopy we used white light and a 100× objective lens. All measurements were performed in air at ~25 °C and atmospheric pressure.

Transmission Electron Microscopy Characterization. We used a Shottky field emission equipped high-resolution transmission electron microscope (JEOL 2010F, 200 keV) to study the effect of our defect treatment on the structure of the TMD monolayers. We employed a polymer-free transfer method to prepare suspended TMD samples for HRTEM imaging. Once a suitable WS_2 monolayer was identified, it was cleaned in *n*-methylpyrrolidone and 2-propanol and dried in N_2. A 300-mesh Cu grid with a carbon film containing 2 μm holes (Quantifoil) was placed directly over the monolayer WS_2 flake on a SiO_2/Si wafer with the carbon grid facing the wafer. A drop of 2-propanol was deposited directly over the TEM grid, pulling it into contact with the monolayers while naturally drying. We heated the adhered grid at 120 °C for at least 20 min to remove residual water or solvent. Once cooled to room temperature, the underlying SiO_2 film was completely etched away by concentrated (49%) hydrofluoric acid, releasing the TEM grid/WS_2 from the silicon wafer. The floating grid was cleaned in a deionized water bath and dried in air. The TEM grid was heated in a vacuum oven for several days at 120 °C to remove residual water/solvent/polymer residue and to prevent the buildup of contamination. All processing was performed under Class 100 cleanroom conditions except for ~5 min of TEM sample loading time.

Conflict of Interest: The authors declare no competing financial interest.

Acknowledgment. N.K. acknowledges funding from the USA National Science Foundation (Awards 1234641 and 1435783) and the John A. Clark and Edward T. Crossan chair professorship at the Rensselaer Polytechnic Institute.

Supporting Information Available: Analysis of the PL defect profiles obtained in ref 14 after normalization of the results, Raman and photoluminescence spectra, normalized to the intensity of the WS_2 in-plane Raman modes, for the sample tested in Figure 2, test data showing the reproducibility of our results on a different monolayer WS_2 sample, and TEM simulation of sulfur and tungsten vacancies in the WS_2 lattice. This material is available free of charge *via* the Internet at http://pubs.acs.org.

REFERENCES AND NOTES

1. Splendiani, A.; Sun, L.; Zhang, Y.; Li, T.; Kim, J.; Chim, C.-Y.; Galli, G.; Wang, F. Emerging Photoluminescence in Monolayer MoS_2. *Nano Lett.* **2010**, *10*, 1271–1275.
2. Mak, K. F.; Lee, C.; Hone, J.; Shan, J.; Heinz, T. F. Atomically Thin MoS_2: A New Direct-Gap Semiconductor. *Phys. Rev. Lett.* **2010**, *105*, 136805.
3. Elías, A. L.; Perea-López, N.; Castro-Beltrán, A.; Berkdemir, A.; Lv, R.; Feng, S.; Long, A.; Hayashi, T.; Kim, Y. A.; Endo, M.; *et al.* Controlled Synthesis and Transfer of Large Area WS_2 Sheets: From Single-Layer to Few-Layers. *ACS Nano* **2013**, *7*, 5235–5242.
4. Lopez-Sanchez, O.; Lembke, D.; Kayci, M.; Radenovic, A.; Kis, A. Ultrasensitive Photodetectors Based on Monolayer MoS_2. *Nat. Nanotechnol.* **2013**, *8*, 497–501.
5. Britnell, L.; Ribeiro, R. M.; Eckmann, A.; Jalil, R.; Belle, B. D.; Mishchenko, A.; Kim, Y.-J.; Gorbachev, R. V.; Georgiou, T.; Morozov, S. V.; *et al.* Strong Light-Matter Interactions in Heterostructures of Atomically Thin Films. *Science* **2013**, *340*, 1311–1314.
6. Ross, J. S.; Wu, S.; Yu, H.; Ghimire, N. J.; Jones, A. M.; Aivazian, G.; Yan, J.; Mandrus, D. G.; Xiao, D.; Yao, W.; *et al.* Electrical

Control of Neutral and Charged Excitons in a Monolayer Semiconductor. *Nat. Commun.* **2013**, *4*, 1474.
7. Mitioglu, A.; Plochocka, P.; Jadczak, J.; Escoffier, W.; Rikken, G.; Kulyuk, L.; Maude, D. Optical Manipulation of the Exciton Charge State in Single-Layer Tungsten Disulfide. *Phys. Rev. B* **2013**, *88*, 245403.
8. Jones, A. M.; Yu, H.; Ghimire, N. J.; Wu, S.; Aivazian, G.; Ross, J. S.; Zhao, B.; Yan, J.; Mandrus, D. G.; Xiao, D.; *et al*. Optical Generation of Excitonic Valley Coherence in Monolayer WSe_2. *Nat. Nanotechnol.* **2013**, *8*, 634–638.
9. Eksik, O.; Gao, J.; Shojaee, S.; Thomas, A.; Chow, P.; Bartolucci, S.; Lucca, D.; Koratkar, N. Epoxy Nanocomposites with Two-Dimensional Transition Metal Dichalcogenide Additives. *ACS Nano* **2014**, *8*, 5282–5289.
10. Radisavljevic, B.; Kis, A. Mobility Engineering and a Metal−Insulator Transition in Monolayer MoS_2. *Nat. Mater.* **2013**, *12*, 815–820.
11. Mouri, S.; Miyauchi, Y.; Matsuda, K. Tunable Photoluminescence of Monolayer MoS_2 *via* Chemical Doping. *Nano Lett.* **2013**, *13*, 5944–5948.
12. Zandiatashbar, A.; Lee, G.-H.; An, S. J.; Lee, S.; Mathew, N.; Terrones, M.; Hayashi, T.; Picu, C. R.; Hone, J.; Koratkar, N. Effect of Defects on the Intrinsic Strength and Stiffness of Graphene. *Nat. Commun.* **2014**, *5*, 3186.
13. Ferrari, A. C.; Meyer, J. C.; Scardaci, V.; Casiraghi, C.; Lazzeri, M.; Mauri, F.; Piscanec, S.; Jiang, D.; Novoselov, K. S.; Roth, S.; *et al*. Raman Spectrum of Graphene and Graphene Layers. *Phys. Rev. Lett.* **2006**, *97*, 187401.
14. Tongay, S.; Suh, J.; Ataca, C.; Fan, W.; Luce, A.; Kang, J. S.; Liu, J.; Ko, C.; Raghunathanan, R.; Zhou, J.; *et al*. Defects Activated Photoluminescence in Two-Dimensional Semiconductors: Interplay between Bound, Charged, and Free Excitons. *Sci. Rep.* **2013**, *3*, 2657.
15. Zhao, W.; Ghorannevis, Z.; Amara, K. K.; Pang, J. R.; Toh, M.; Zhang, X.; Kloc, C.; Tan, P. H.; Eda, G. Lattice Dynamics in Mono- and Few-Layer Sheets of WS_2 and WSe_2. *Nanoscale* **2013**, *5*, 9677–9683.
16. Berkdemir, A.; Gutiérrez, H. R.; Botello-Méndez, A. R.; Perea-López, N.; Elías, A. L.; Chia, C.-I.; Wang, B.; Crespi, V. H.; López-Urías, F.; Charlier, J.-C.; *et al*. Identification of Individual and Few Layers of WS_2 Using Raman Spectroscopy. *Sci. Rep.* **2013**, *3*, 1755.
17. Zhao, W.; Ghorannevis, Z.; Chu, L.; Toh, M.; Kloc, C.; Tan, P.-H.; Eda, G. Evolution of Electronic Structure in Atomically Thin Sheets of WS_2 and WSe_2. *ACS Nano* **2013**, *7*, 791–797.
18. Beal, A. R.; Knights, J. C.; Liang, W. Y. Transmission Spectra of Some Transition Metal Dichalcogenides. II. Group VIA: Trigonal Prismatic Coordination. *J. Phys. C: Solid State Phys.* **1972**, *5*, 3540–3551.
19. Zhao, W.; Ribeiro, R. M.; Toh, M.; Carvalho, A.; Kloc, C.; Castro Neto, A. H.; Eda, G. Origin of Indirect Optical Transitions in Few-Layer MoS_2, WS_2, and WSe_2. *Nano Lett.* **2013**, *13*, 5627–5634.
20. Mak, K. F.; He, K.; Lee, C.; Lee, G. H.; Hone, J.; Heinz, T. F.; Shan, J. Tightly Bound Trions in Monolayer MoS_2. *Nat. Mater.* **2013**, *12*, 207–211.
21. Chernikov, A.; Berkelbach, T. C.; Hill, H. M.; Rigosi, A.; Li, Y.; Aslan, O. B.; Reichman, D. R.; Hybertsen, M. S.; Heinz, T. F. Exciton Binding Energy and Nonhydrogenic Rydberg Series in Monolayer WS_2. *Phys. Rev. Lett.* **2014**, *113*, 076802.
22. Chen, J.-H.; Jang, C.; Adam, S.; Fuhrer; Williams, E. D.; Ishigami, M. Charged-Impurity Scattering in Graphene. *Nat. Phys.* **2008**, *4*, 377–381.
23. Conley, H. J.; Wang, B.; Ziegler, J. I.; Haglund, R. F.; Pantelides, S. T.; Bolotin, K. I. Bandgap Engineering of Strained Monolayer and Bilayer MoS_2. *Nano Lett.* **2013**, *13*, 3626–3630.
24. Akimoto, K.; Tamamura, K.; Ogawa, J.; Mori, Y.; Kojima, C. Photoluminescence Study on the Interface of a GaAs/AlxGa1-xAs Heterostructure Grown by Metalorganic Chemical Vapor Deposition. *J. Appl. Phys.* **1988**, *63*, 460.
25. Kaftelen, H.; Ocakoglu, K.; Thomann, R.; Tu, S.; Weber, S.; Erdem, E. EPR and Photoluminescence Spectroscopy Studies on the Defect Structure of ZnO Nanocrystals. *Phys. Rev. B* **2012**, *86*, 014113.
26. Nan, H.; Wang, Z.; Wang, W.; Liang, Z.; Lu, Y.; Chen, Q.; He, D.; Tan, P.; Miao, F.; Wang, X.; *et al*. Strong Photoluminescence Enhancement of MoS_2 through Defect Engineering and Oxygen Bonding. *ACS Nano* **2014**, *8*, 5738–5745.
27. Van der Zande, A. M.; Huang, P. Y.; Chenet, D. A.; Berkelbach, T. C.; You, Y.; Lee, G.-H.; Heinz, T. F.; Reichman, D. R.; Muller, D. A.; Hone, J. C. Grains and Grain Boundaries in Highly Crystalline Monolayer Molybdenum Disulphide. *Nat. Mater.* **2013**, *12*, 554–561.
28. Gutiérrez, H. R.; Perea-López, N.; Elías, A. L.; Berkdemir, A.; Wang, B.; Lv, R.; López-Urías, F.; Crespi, V. H.; Terrones, H.; Terrones, M. Extraordinary Room-Temperature Photoluminescence in Triangular WS_2 Monolayers. *Nano Lett.* **2013**, *13*, 3447–3454.
29. Brivio, J.; Alexander, D. T. L.; Kis, A. Ripples and Layers in Ultrathin MoS_2 Membranes. *Nano Lett.* **2011**, *11*, 5148–5153.
30. Komsa, H.-P.; Kotakoski, J.; Kurasch, S.; Lehtinen, O.; Kaiser, U.; Krasheninnikov, A. V. Two-Dimensional Transition Metal Dichalcogenides under Electron Irradiation: Defect Production and Doping. *Phys. Rev. Lett.* **2012**, *109*, 035503.
31. Ovchinnikov, D.; Allain, A.; Huang, Y.-S.; Dumcenco, D.; Kis, A. Electrical Transport Properties of Single-Layer WS_2. *ACS Nano* **2014**, *8*, 8174–8181.
32. Kang, N.; Paudel, H. P.; Leuenberger, M. N.; Tetard, L.; Khondaker, S. I. Photoluminescence Quenching in Single-Layer MoS_2 *via* Oxygen Plasma Treatment. *J. Phys. Chem. C* **2014**, *118*, 21258–21263.